CHALMERS
UNIVERSITY OF TECHNOLOGY

Modelling, design and optimisation of connected array antennas

Master's thesis in Applied Physics

ERIK PAYERL

Department of Signals and systems
CHALMERS UNIVERSITY OF TECHNOLOGY
Göteborg, Sweden 2016

Master's thesis 2016:EX090

Modelling, design and optimisation of connected array antennas

ERIK PAYERL

Department of Signals and systems
Signal processing research group
Chalmers University of Technology
Göteborg, Sweden 2016

Modelling, design and optimisation of connected array antennas
ERIK PAYERL

Supervisor: Thomas Rylander, Department of Signals and systems
Examiner: Thomas Rylander

Master's Thesis 2016:EX090
Department of Signals and systems
Signal processing research group
Chalmers University of Technology
SE-412 96 Göteborg
Telephone +46 31 772 1000

Typeset in LaTeX
Göteborg, Sweden 2016

Modelling, design and optimisation of connected array antennas
ERIK PAYERL
Department of Signals and systems
Chalmers University of Technology

Abstract

Wideband and widescan array antennas are attractive since they offer multi-function capabilities with a single aperture. In particular, connected array antennas are interesting as they provide broad-band operation in combination with low cross-polarisation. In this thesis, we present a electrically thin connected slot array with dielectric superstrates. The antenna is analysed with the finite element method, where the computational domain is the unit cell of an infinite array antenna. An optimization of the connected array design is performed based on a finite-difference gradient of an objective function with respect to the design parameters. The proposed design achieves more than one octave bandwidth ($6.5 - 14.5\,\mathrm{GHz}$) within a scanning range of $\pm 60°$ in all azimuth planes.

Keywords: Connected arrays, wideband arrays, wide-scan array

Contents

1

Introduction

1.1 Wideband and widescan array antennas

Array antennas are receiving great attention, both for military and commercial applications. The possibility of the array antenna to steer the beam electronically is one of the key points to tackle the exponential increase of data traffic in mobile communication system [1]. Wideband and widescan array antennas are further attractive since they offer multi-function capabilities with a single antenna aperture. They can simultaneously accommodate multiple frequency bands, beams and polarizations in order to consolidate multiple antenna functions into a antenna. This can be especially useful in situations where space and weight are major constraints. The ideal antenna would be one that is thin and easy to manufacture with wideband, widescan and good polarization purity properties.

Common antenna designs for wideband and widescanning arrays are stacked patches, tapered slot (Vivaldi) antennas [2] and connected arrays. In particular, connected array antennas are interesting as they provide broad-band operation in combination with low cross-polarisation. A connected array antenna consists of antenna elements (typically dipoles or slots) that are strongly coupled to each other, which can be realised by electrical connection. Thus, a connected array antenna can be considered to be a single antenna that is periodically fed, which allows for currents that are nearly constant with frequency. (In contrast, a conventional array antenna is composed of resonant antenna elements that are separated from each other, which limits the frequency range of operation.) The radiating currents mainly flow along the aperture plane with no substantial vertical component, which allow for good polarization purity.

A backing reflector is necessary to ensure unidirectional radiation. However, this degrades the bandwith of the antenna due to resonances and inductance introduced by the ground plane. The inductive ground plane loading can be mitigated with strong capacitive coupling between the elements such as the exhibited in a tightly coupled dipole array. A planar dual-polarized antenna that utilises this concept is presented in Refs. [3] [4] and it achieves a voltage standing wave ration (VSWR) < 2.6 in the frequency range $3.53 - 21.2\,\mathrm{GHz}$ within a scanning range of $\pm 45°$. Another way to mitigate the performance degradation due to a backing reflector is to introduce lossy materials to suppress resonances from the introduction of a ground plane. An example of this is presented in Refs. [5] where connected slots loaded with artificial dielectric superstrates demonstrate a performance of VSWR < 2 for $6.5 - 14.5\,\mathrm{GHz}$ within a scanning range of $\pm 50°$ in all azimuth planes. Both concepts of tightly coupled dipoles and dielectric superstrates has been combined in Ref. [6] to achieve a dual-polarized antenna with VSWR less than 2 for the frequency band $3.25 - 18\,\text{GHz}$ with scan angles up to $50°$ in all planes.

1.2 Purpose

The purpose of this thesis is to study a connected array antenna design with dielectric superstrates, where its feeding structure is incorporated. The connected array antenna should feature broad frequency-band operation and, simultaneously, allow for large scanning angles.

1.3 Scope

- The antenna analysis is restricted to a unit cell, i.e. the antenna is be modelled as an infinite array.
- The antenna is fed by a coaxial waveguide.
- The analysis is restricted to linear electromagnetic phenomena.
- The antenna is modelled from its port to its radiated wave.
- Only one antenna design is optimised.

1.4 Objective

The objective is to find a connected array antenna design with its feeding structure such that it is possible to realise the antenna on layered substrates.

2
Antenna description

2.1 Planar rectangular array antennas

Consider a planar array antenna with $M \times N$ identical antenna elements. The antenna elements are placed on a rectangular grid in the xy-plane with element spacing L_x in the x-direction and L_y in the y-direction. The elements are translated relative each other with the positions given by $\boldsymbol{r}_{mn} = \hat{\boldsymbol{x}} m L_x + \hat{\boldsymbol{y}} n L_y$ with $m = 1, \ldots, M$ and $n = 1, \ldots, N$. Such an array antenna is shown in Figure 2.1.

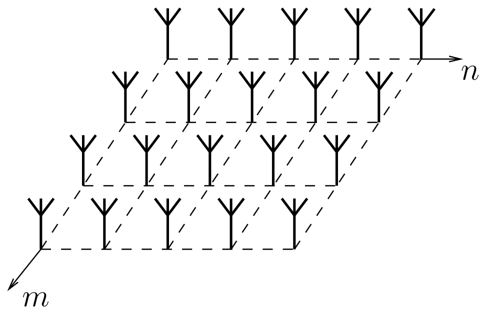

Figure 2.1: A planar rectangular array antenna with $M \times N$ identical antenna elements. The elements are translated with respect to each other.

2.2 Radiated electromagnetic field

One of the most important properties of planar array antennas is the capability to change the form and direction of the radiating field by steering the phase and amplitude on the ports of the antenna elements. At large enough distance r from the antenna, in the so-called far-field region, the radiated electric field becomes separable according to

$$\boldsymbol{E}(r, \theta, \phi) = \frac{e^{-jkr}}{r} \boldsymbol{G}(\theta, \phi) \tag{2.1}$$

where $\boldsymbol{G}(\theta, \phi)$ is the complex radiation field function. For the planar rectangular array antenna described in section 2.1, the radiation field of element (m, n) at point $\boldsymbol{r}$ is

$$\boldsymbol{E}_{mn}(r, \theta, \phi) = \frac{e^{-jkr}}{r} \boldsymbol{G}(\theta, \phi) e^{jk\boldsymbol{r}_{mn} \cdot \hat{\boldsymbol{r}}} \tag{2.2}$$

where $\boldsymbol{G}(\theta, \phi)$ is the radiation field function when referred to the phase reference point $\boldsymbol{r}_{mn}$ of the individual element. The factor $e^{jk\boldsymbol{r}_{mn} \cdot \hat{\boldsymbol{r}}}$ shifts the phase reference point to the origin of the coordinate system of the whole antenna. By superposition of the field contributions from the individual elements, we get the radiation field function for the array

$$\boldsymbol{G}_{\mathrm{A}}(\theta,\phi) = \sum_{mn} \boldsymbol{G}(\theta,\phi) A_{mn} e^{j\Phi_{mn}} e^{jk\boldsymbol{r}_{mn}\cdot\hat{\boldsymbol{r}}} \tag{2.3}$$

where A_{mn} and Φ_{mn} are the amplitude and phase excitation of element (m,n). The array radiation field function can be written as a product or the element radiation field function and the array factor AF, according to

$$\boldsymbol{G}_{\mathrm{A}}(\theta,\phi) = \boldsymbol{G}(\theta,\phi) AF(\theta,\phi) \tag{2.4}$$

where

$$AF(\theta,\phi) = \sum_{mn} A_{mn} e^{j\Phi_{mn}} e^{jk\boldsymbol{r}_{mn}\cdot\hat{\boldsymbol{r}}} \tag{2.5}$$

To see how the array factor $AF(\theta,\phi)$ varies with the scan angle (θ,ϕ), we can write $AF(\theta,\phi)$ in terms of the Fourier transform of the amplitude excitation, i.e. as an infinite sum of so-called Floquet modes. To do this, we first need to write amplitude excitation A_{mn} as continuous and smooth distribution

$$A(\boldsymbol{r}) = A_{mn} \quad \text{for} \quad \boldsymbol{r} = \boldsymbol{r}_{mn} \tag{2.6}$$

Similarly we introduce a smooth and continuous phase excitation distribution $\Phi(x,y)$ that we assume varies linearly as

$$\Phi(x,y) = \Phi_{\mathrm{c}} - k_x^{\mathrm{s}} x - k_y^{\mathrm{s}} y \tag{2.7}$$

where k_x^{s} and k_y^{s} are the propagation constants for the phase in the x- and y-directions. Φ_{c} is a constant phase offset.

The array factor can now be written as a double integral by using the sampling properties of the delta function

$$A(\boldsymbol{r}) = \int_{-\infty}^{\infty}\int_{-\infty}^{\infty} \left\{ \sum_{n=-\infty}^{\infty} \delta(y - nL_y) \sum_{m=-\infty}^{\infty} \delta(x - mL_x) \right\} A(x,y) e^{j\Phi(x,y)} e^{jk\boldsymbol{r}\cdot\hat{\boldsymbol{r}}} \,\mathrm{d}x\,\mathrm{d}y \tag{2.8}$$

where $\boldsymbol{r} = x\hat{\boldsymbol{x}} + y\hat{\boldsymbol{y}}$. It is posible to extend the element by element sums to infinity as $A(x,y)$ is zero where $n < 1$, $n > N$, $m < 1$ and $m > M$. The delta series in both the x- and y-directions are periodic with respect to L_x and L_y and can thus be expanded in Fourier series. This allows us to finally write the array factor as an infinite sum of the so-called Floquet modes

$$AF(\theta,\phi) = e^{j\Phi_{\mathrm{c}}} \frac{1}{L_x L_y} \sum_{p=-\infty}^{\infty} \sum_{q=-\infty}^{\infty} \tilde{A}(k_x - k_{xp}, k_y - k_{yq}) \tag{2.9}$$

where

$$\tilde{A}(k_x,k_y) = \int_{-\infty}^{\infty}\int_{-\infty}^{\infty} A(x,y) e^{jk_x x} e^{jk_y y} \,\mathrm{d}x\,\mathrm{d}y \tag{2.10}$$

is the Fouries transform of the amplitude excitation and

$$k_{xp} = k_x^{\mathrm{s}} + \frac{2\pi p}{L_x} \tag{2.11}$$

$$k_{yq} = k_x^{\mathrm{s}} + \frac{2\pi q}{L_y} \tag{2.12}$$

are the phase difference between neighbouring elements.

Each term in the sum (2.9) has a maximum at $(k_x = k_{xp}, k_y = k_{yq})$. The first maximum at $p = q = 0$ corresponds to the main radiating antenna lobe and the other maxima are grating lobes. If the array spacing L_x and L_y are smaller than $\lambda_0/2$ no grating lobes occur. The array factor for the main lobe has its maximum for

$$k_{x0} = k_x^{\mathrm{s}}, \quad k_{y0} = k_y^{\mathrm{s}} \tag{2.13}$$

It is thus possible to steer the main lobe at a scan angle $(\theta_{\mathrm{s}}, \phi_{\mathrm{s}})$ through the phase propagation constant. The wave vector of the main lobe is

$$\boldsymbol{k} = \hat{x}k_x^{\mathrm{s}} + \hat{y}k_y^{\mathrm{s}} + \hat{z}k_z \tag{2.14}$$

with

$$k_x^{\mathrm{s}} = k_0 \cos(\phi_{\mathrm{s}}) \sin(\theta_{\mathrm{s}}) \tag{2.15}$$

$$k_y^{\mathrm{s}} = k_0 \sin(\phi_{\mathrm{s}}) \sin(\theta_{\mathrm{s}}) \tag{2.16}$$

$$k_z = k_0 \cos(\theta_{\mathrm{s}}) \tag{2.17}$$

and $k_0 = \omega/c_0$.

2.3 Active reflection coefficient

Impedance mismatch between the feed line and the antenna leads to unwanted reflections and power loss. The active antenna element impedance (as seen by the feed line) does not only depend on the element itself, but also on the mutual coupling between the elements. The reflected wave amplitude on the port of array element i can be expressed as

$$V_i^- = V_i^+ \cdot S_{ii} + \sum_{j \neq i} V_j^+ \cdot S_{ij} \tag{2.18}$$

where V_j^+ is the excitation of array element j and S_{ij} are the scattering parameters. To simplify the notation we use a linear index $i \leftrightarrow (m, n)$ for the array elements where $i = N(n-1) + m$. The active reflection coefficient for element i is given by

$$\mathit{\Gamma}_i = \frac{V_i^-}{V_i^+} = S_{ii} + \sum_{j \neq i} \frac{V_j^+}{V_i^+} S_{ij} \tag{2.19}$$

Another often used measue of the impedance mismatch is the so called *voltage standing wave ration* defined as

$$VSWR = \frac{1 + |\mathit{\Gamma}|}{1 - |\mathit{\Gamma}|} \tag{2.20}$$

2.4 Co- and cross-polarization

The radiating far-field has two orthogonal components along θ and ϕ. The co-polarisation vector is defined as the desired polarisation of the electric field. The cross-polarisation vector represent undesired polarisation and is orthogonal to the co-polarisation vector. For an antenna with a transmitted field polarized in the $\hat{y}$-direction at $\theta = 0$, the co- and cross-polarizations vectors are according to the third definition from Ludvig [7] defined as

$$\hat{\boldsymbol{i}}_{\text{co}} = \sin(\phi)\hat{\boldsymbol{i}}_\theta + \cos(\phi)\hat{\boldsymbol{i}}_\phi \tag{2.21}$$

$$\hat{\boldsymbol{i}}_{\text{cross}} = \cos(\phi)\hat{\boldsymbol{i}}_\theta - \sin(\phi)\hat{\boldsymbol{i}}_\phi \tag{2.22}$$

with

$$\hat{\boldsymbol{i}}_\theta = \hat{\boldsymbol{x}}\cos(\theta)\cos(\phi) + \hat{\boldsymbol{y}}\cos(\theta)\sin(\phi) - \hat{\boldsymbol{z}}\sin(\theta) \tag{2.23}$$

$$\hat{\boldsymbol{i}}_\phi = -\hat{\boldsymbol{x}}\sin(\phi) + \hat{\boldsymbol{y}}\cos(\phi) \tag{2.24}$$

The co-polarized and cross-polarized components of an electric field $\boldsymbol{E}$ are thus defined as

$$E_{\text{co}} = \boldsymbol{E} \cdot \hat{\boldsymbol{i}}_{\text{co}} \tag{2.25}$$

$$E_{\text{cross}} = \boldsymbol{E} \cdot \hat{\boldsymbol{i}}_{\text{cross}} \tag{2.26}$$

2.5 Material characterization of antennas

2.5.1 Metal

In a perfect electric conductor, the field penetration is zero for all frequencies. Perfect electric conductors can thus entirely be excluded from the calculation domain when boundary value problem of the electric fields is solved. While no truly perfect conductors exists in nature, good conductors can still be excluded from the computational domain if appropriate boundary conditions are applied. We derive such boundary conditions by assuming the following:

1. The loss tangent of the material is high (i.e. a high loss dialectic or a conductor). As a consequence the wave length and skin depth inside the material is small.

2. The radii of curvature must be large compared to the skin depth. The fields vary thus only slowly from point to point on the surface.

3. There are no sources within the medium.

Under these conditions, as a first order approximation, the fields inside the medium relate to each other as in any plane wave and both the $\boldsymbol{E}$ and $\boldsymbol{H}$ field are parallel to the surface of the material [8]. From continuity at a planar boundary we get

$$\hat{\boldsymbol{n}} \times \boldsymbol{E} = -\eta(\hat{\boldsymbol{n}} \times (\hat{\boldsymbol{n}} \times \boldsymbol{H})) \tag{2.27}$$

where η is the surface impedance. This can be taken as a boundary condition and is often called impedance boundary condition or the Leontovich condition [9]. Ohmic losses due to the finite conductivity of metals will be denoted P_{m}.

2.5.2 Dielectric medium

Losses in dielectric media are accounted for by a complex relative permittivity

$$\varepsilon = \varepsilon' - j\varepsilon'' \tag{2.28}$$

The imaginary part can also be expressed with

$$\varepsilon = \varepsilon'(1 - j\tan\delta) \tag{2.29}$$

where $\tan\delta = \varepsilon''/\varepsilon'$ is called dissipation factor or loss tangent. The power dissipated due to dielectric losses will from here on be denoted P_{d} and calculated as

$$P_{\mathrm{d}} = \int_V Re\{\boldsymbol{E} \cdot \boldsymbol{J}\} \tag{2.30}$$

2.5.3 Artificial dielectrics

Layers of dielectric media can support surface waves and a significant amount of power can be lost in such waves. This loss may be reduced with artificial dielectric layers (ADLs) [10]. An ADL consists of metallic structures embedded in a host material. If these structures and the spacing between such structures are small compared to the wavelength within the resulting dielectric media, the ADL can be described as an equivalent anisotropic dielectric medium with an effective permittivity $\boldsymbol{\varepsilon}_{\mathrm{eff}}$. With an ADL consisting of horizontally placed metal patches, the effective permittivity largely increases for a field with normal incidence to the patches. When the electric field is orthogonal to the metal patches, the equivalent dielectric approaches the dielectric constant of the host material. Lower $\varepsilon_{\mathrm{eff}}$ for high angles of incidence implies much lower surface wave excitation.

2.6 Connected slot array antenna design

In this section, we present the nominal antenna design studied in this thesis. The antenna is a single-polarized connected slot array antenna loaded with three dielectric layers. The antenna is placed above a backing reflector (ground plane) to ensure unidirectional radiation. The purpose of the dielectric layers is to reduce the performance degradation due to the presence of the backing reflector. Figure 2.2 shows the different layers of the antenna with the respective geometrical parameters. The dimension of the dielectric slabs are listed in Table 2.1 and other dimensions in Table 2.2. Figure 2.3 shows a 3D view of the entire unit cell. Two dielectric substrates occupy the space between the backing reflector and the array plane, *sub1* of relative permittivity $\varepsilon_r = 1.4$ and *sub2* closest to the array plane of relative permittivity $\varepsilon_r = 2.2$. The loss tangent in both the dielectric substrates and the dielectric superstrates is set to $\tan\delta = 0.02$.

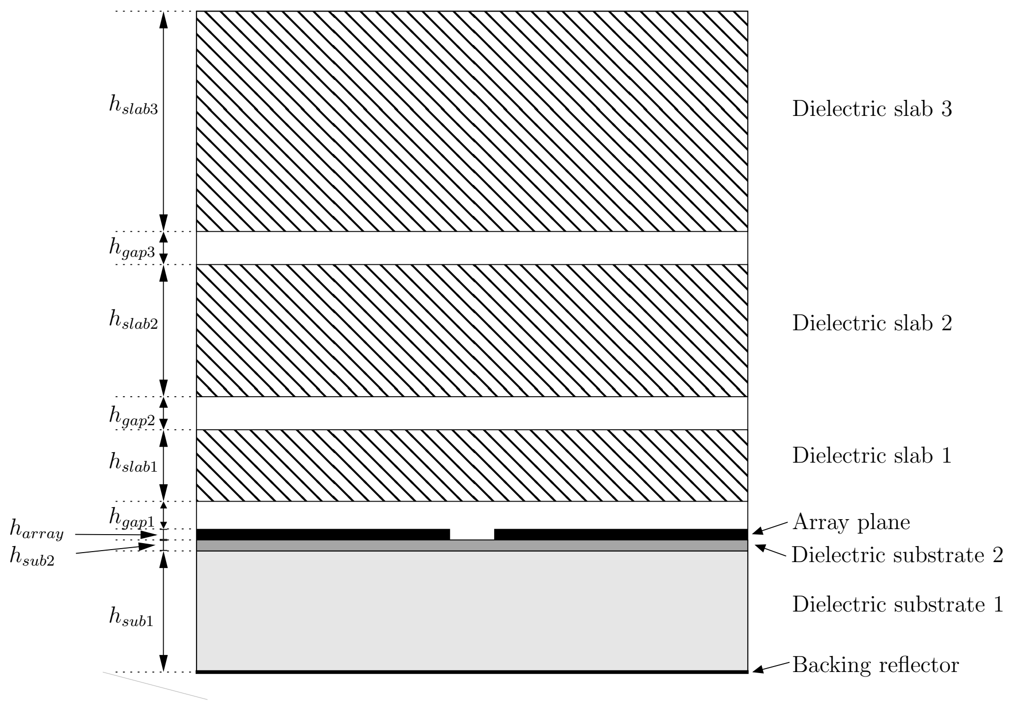

Figure 2.2: A schematic view of the different layers and distance in the antenna.

Table 2.1: Dimensions of the three dielectric slabs.

Parameter	*Unit*	*Slab1*	*Slab2*	*Slab3*
h_{slab}	(mm)	0.635	1.998	1.998
h_{gap}	(mm)	0.254	0.5	0.33
ε_r	-	16.5	5.5	1.72

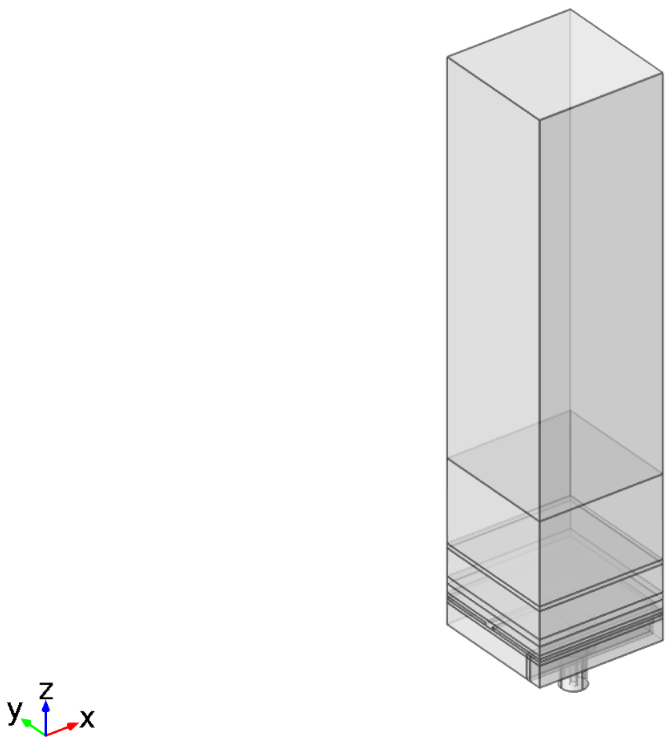

Figure 2.3: 3D view of the antenna unit cell.

The feeding structure is shown in Figure 2.4. A coaxial waveguide port is located under the backing reflector. This connects to a microstrip line feeding the slot elements through a coaxial-to-microstrip transition. The microstrip feed line is terminated with a shorting via. A conducting wall is included between the slots to suppress common-mode current excitation.

Table 2.2: Dimensions of the array unit cell in Figure 2.2

L_x	$= 9.31\,\mathrm{mm}$	Width of the unit cell, $L_x = L_y$
L_z	$= 39.97\,\mathrm{mm}$	Height of the unit cell
h_{array}	$= 0.2\,\mathrm{mm}$	Height of array plane
h_{sub1}	$= 1.546\,\mathrm{mm}$	Height of substrate one
h_{sub2}	$= 0.254\,\mathrm{mm}$	Height of substrate two
w_{s}	$= 0.7\,\mathrm{mm}$	Width of slot
l_{feed}	$= 3.58\,\mathrm{mm}$	Length of microstrip feed line

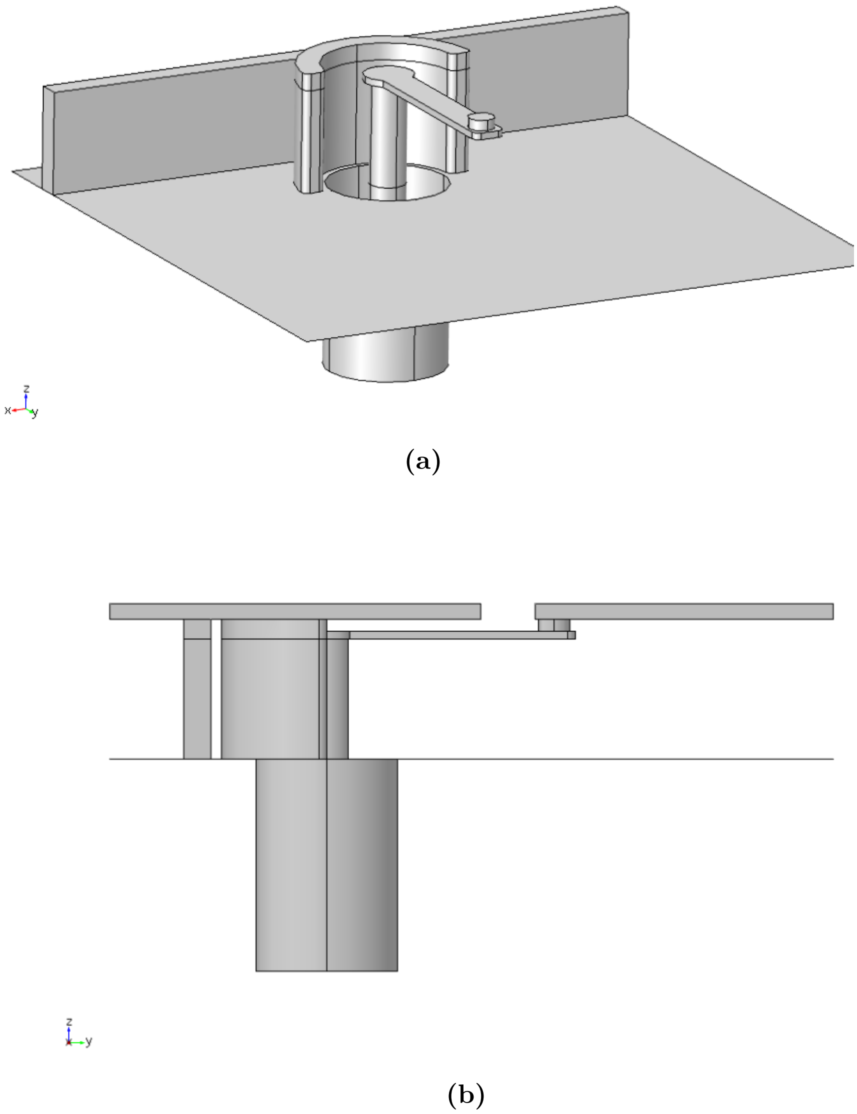

Figure 2.4: The metal parts of the antenna consisting of ground plane, coaxial port and feeding structure. The array plane is hidden in (a) but included in (b).

3

Computational method

3.1 The antenna boundary value problem

The electromagnetic environment for an interior element of a large finite array, can be well approximated by an infinite array antenna. To compute the electromagnetic field for the interior elements of a large finite array, it is thus enough to consider a single unit cell with periodic boundary conditions. Such a unit cell with a coaxial feed is shown in Figure 3.1.

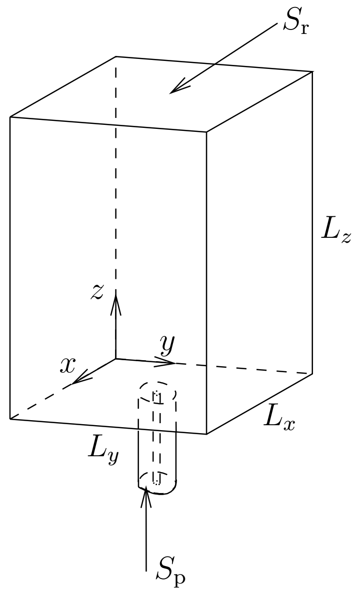

Figure 3.1: A unit cell of an infinite group antenna with coaxial feed. The surface of the coaxial port is denoted S_p. The surface truncating the computational domain is denoted S_r.

The electric field of the infinite array can be calculated by solving the corresponding frequency-domain boundary value problem given by equation (3.5) to (3.10). Let V denote the volume of the unit cell in Figure 3.1 and V_m the volume of the metal parts of the antenna. To simplify the calculations, the wave equation (3.5) is solved only in the non-metal domains $V \setminus V_\mathrm{m}$. To model the metal, an impedance boundary condition (3.6) is used on the surface of the metal domains S_m, which accounts for ohmic losses. Losses in non-metal domains are accounted for by the complex permittivity ε_c. The unit cell is repeated to infinity in the x- and y-direction through the periodic Flouqet boundary conditions (3.7) and (3.8), where the direction of the main lobe is specified by

$$k_x = k_0 \cos(\phi_\mathrm{s}) \sin(\theta_\mathrm{s}) \tag{3.1}$$
$$k_y = k_0 \sin(\phi_\mathrm{s}) \sin(\theta_\mathrm{s}) \tag{3.2}$$
$$k_z = k_0 \cos(\theta_\mathrm{s}) \tag{3.3}$$
$$\tag{3.4}$$

and $k_0 = \omega/c_0$. On the bottom of the unit cell, we find the coaxial port and a metal ground plane. On the coaxial port surface S_p, we use the Robbin boundary condition (3.9). The boundary condition (3.10) applied on the top surface S_r of the unit cell will be derived in section 3.2.1.

$$\nabla \times (\nabla \times \boldsymbol{E}) - \omega^2 \mu_0 \varepsilon_\mathrm{c} \boldsymbol{E} = \boldsymbol{0} \quad \text{in } V \setminus V_\mathrm{m} \tag{3.5}$$
$$\sqrt{\mu_0/\varepsilon_\mathrm{c}}\, \hat{\boldsymbol{n}} \times \boldsymbol{H} + \hat{\boldsymbol{n}} \times (\hat{\boldsymbol{n}} \times \boldsymbol{E}) = \boldsymbol{0} \quad \text{on } S_\mathrm{m} \tag{3.6}$$
$$\boldsymbol{E}(0, y, z) e^{-jk_x L_x} = \boldsymbol{E}(L_x, y, z) \tag{3.7}$$
$$\boldsymbol{E}(x, 0, z) e^{-jk_y L_y} = \boldsymbol{E}(x, L_y, z) \tag{3.8}$$
$$\hat{\boldsymbol{n}} \times (\nabla \times \boldsymbol{E}) + jk_c \hat{\boldsymbol{n}} \times (\hat{\boldsymbol{n}} \times \boldsymbol{E}) = Zjk_c \hat{\boldsymbol{n}} \times (\hat{\boldsymbol{n}} \times \boldsymbol{E}_\mathrm{i}) \quad \text{on } S_\mathrm{p} \tag{3.9}$$
$$\hat{\boldsymbol{n}} \times (\nabla \times \boldsymbol{E}) + jk_0 \hat{\boldsymbol{n}} \times (\hat{k}_{00} \times \boldsymbol{E}) = \boldsymbol{0} \quad \text{on } S_\mathrm{r} \tag{3.10}$$

3.2 Finite element method

The electromagnetic field $\boldsymbol{E}$ in Eq. (3.5) – (3.10) can be computed numerically by the finite element method (FEM). The general recipe to solve a differential equation $\boldsymbol{L}[\boldsymbol{E}] = \boldsymbol{s}$ by FEM is to divide the computational domain into cells, which is referred to as a mesh. We approximate the solution by expanding the unknown function $\boldsymbol{E}$ in a finite number of basis functions. The so-called *edge elements* $N_j(\boldsymbol{r})$ are very well-suited for approximating electromagnetic fields [11]. The electric field is expressed as

$$\boldsymbol{E}(\boldsymbol{r}) = \sum_{j=1}^{N_\mathrm{edge}} E_j \boldsymbol{N}_j(\boldsymbol{r}) \tag{3.11}$$

where N_edge is the total number of edges, E_j is the tangential component of $\boldsymbol{E}$ along the j-th edge and $\boldsymbol{N}_j$ is the vector basis function corresponding to the j-th edge. The edge elements $\boldsymbol{N}_j$ are so-called curl-conforming basis functions.

We formulate the residual $\boldsymbol{r} = \boldsymbol{L}[\boldsymbol{E}] - \boldsymbol{s}$ and require it to be zero in the weak sense, i.e. we set the weighted average to zero according to

$$\langle \boldsymbol{W}_i, \boldsymbol{r} \rangle = \int_V \boldsymbol{W}_i \cdot \boldsymbol{r}\, \mathrm{d}V = 0, \quad i = 1, 2, 3, \ldots, n. \tag{3.12}$$

Next, we chose weighting functions $\boldsymbol{W}_i$ and solve for the unknowns E_j. Here, we use Galerkin's method and thus, the weighting functions are chosen from the set of the basis funcion.

The boundary value problem specified by Eq. (3.5) – (3.10) is discretized and solved by FEM by the means of the software COMSOL Multiphysics® [12]. The computational mesh consists of tetrahedral elements and second order curl-conforming basis functions are used. A direct numerical solver is used to solve the FEM system of equations.

3.2.1 Finite element mesh truncation

The infinite space above the antenna (z direction) needs to be truncated into a finite computational domain. We accomplished this by introducing an artificial boundary surface S_r. This artificial boundary should absorb as much as the radiated field as possible to emulate the original free-space environment. There are several approaches to reduce the reflections from such artificial surfaces such as the use of fictional absorbing material layers and the use of surface integral functions [13]. We will here use a mathematical absorbing boundary condition. To derive this boundary condition, we decompose the electric field in plane waves:

$$\boldsymbol{E}(\boldsymbol{r}) = \sum_{pq} \boldsymbol{E}_{pq}^{\mathrm{PW}} e^{-j\boldsymbol{k}_{pq}\cdot\boldsymbol{r}} \tag{3.13}$$

$$\boldsymbol{k}_{pq} = k_0 \hat{k}_{pq} = \hat{x}k_{xp} + \hat{y}k_{yq} + \hat{z}k_z \tag{3.14}$$

where

$$\boldsymbol{E}_{pq}^{\mathrm{PW}} = \frac{e^{jk_z z}}{L_x L_y} \int_{x=-L_x/2}^{L_x/2} \int_{y=-L_y/2}^{L_y/2} \boldsymbol{E}(\xi, \zeta, z) e^{j(k_{xp}\xi + k_{yq}\zeta)} \,\mathrm{d}\xi\,\mathrm{d}\zeta \tag{3.15}$$

This yields

$$\hat{\boldsymbol{n}} \times (\nabla \times \boldsymbol{E}) = \hat{\boldsymbol{n}} \times \left(\sum_{pq} (-j\boldsymbol{k}_{pq}) \times \left(\boldsymbol{E}_{pq}^{\mathrm{PW}} e^{-j\boldsymbol{k}_{pq}\cdot\boldsymbol{r}} \right) \right) \tag{3.16}$$

$$\Rightarrow \hat{\boldsymbol{n}} \times (\nabla \times \boldsymbol{E}) + jk_0 \boldsymbol{\mathcal{L}}(\boldsymbol{E}) = \boldsymbol{0} \tag{3.17}$$

and

$$\boldsymbol{\mathcal{L}}(\boldsymbol{E}) = \hat{\boldsymbol{n}} \times \left[\sum_{pq} \hat{k}_{pq} \times \left(\frac{e^{jk_z z}}{L_x L_y} \int_{x=-L_x/2}^{L_x/2} \int_{y=-L_y/2}^{L_y/2} \boldsymbol{E} e^{j(k_{xp}\xi + k_{yq}\zeta)} \,\mathrm{d}\xi\,\mathrm{d}\zeta \right) \right] \tag{3.18}$$

In the simple case where only the main lobe propagates, $p = q = 0$, this simplifies to the radiating boundary condition given by Eq. (3.10).

4

Results

4.1 Microstrip patch antenna array

In this section, we consider two different infinite equidistant planar arrays of rectangular microstrip patches:

PA. 1 The first problem is an array antenna consisting of $0.3\lambda_0 \times 0.3\lambda_0$ rectangular patches with a period of $0.5\lambda_0$ both in the x and y-direction. Each patch is located at a distance $h = 0.02\lambda_0$ above the ground plane and the substrate between the two has a relative permittivity of $\varepsilon_\mathrm{r} = 2.55$. The antenna is fed by a coaxial port placed $0.075\lambda_0$ from the center of the patch.

PA. 2 The second problem is an array antenna consisting of $0.3\lambda_0 \times 0.3\lambda_0$ rectangular patches with a period of $0.5\lambda_0$ in the x- direction and $0.51\lambda_0$ in the y-direction. Each patch is located at a distance $h = 0.06\lambda_0$ above the ground plane and the substrate has a relative permittivity of $\varepsilon_\mathrm{r} = 2.55$. The antenna is fed by a coaxial port placed $0.14\lambda_0$ from the center of the patch. The spacing between the antenna elements are larger than $\lambda_0/2$ in the y-direction. Thus, it is possible for grating lobes to occur.

Both of these problems have previously been studied by Pozar and Schaubert [14] with a method of moment (MoM) approach. Note that Pozar uses a different definition of the active reflection coefficient:

$$\mathit{\Gamma}_\mathrm{Pozar}(\theta, \phi) = \frac{Z_\mathrm{in}(\theta, \phi) - Z_\mathrm{in}(0,0)}{Z_\mathrm{in}(\theta, \phi) + Z^*_\mathrm{in}(0,0)} \tag{4.1}$$

4.1.1 Plane-wave representation

The element spacing in PA. 1 is small enough to prevent no grating lobes from occurring. Thus, only the main antenna lobe is propagating and it can be represented by a single plane wave in the far-field region.

The radiation boundary condition (3.10), applied to upper surface S_r of the computational domain, is only valid for a single propagating plane wave. Therefore, the truncating surface must be placed in the far-field region. It is thus of importance to know for which height z above the antenna the electric field is well represented by a single plane wave. To investigate this, we formulate the relative difference

$$\delta_\mathrm{rel}(z) = \left[\frac{1}{L_x L_y} \int_{x=-L_x/2}^{L_x/2} \int_{y=-L_y/2}^{L_y/2} \frac{|\boldsymbol{E}^\mathrm{FE}(x,y,z) - \boldsymbol{E}^\mathrm{PW}(x,y,z)|^2}{|\boldsymbol{E}^\mathrm{PW}(x,y,z)|^2} \,\mathrm{d}y\,\mathrm{d}x \right]^{1/2} \tag{4.2}$$

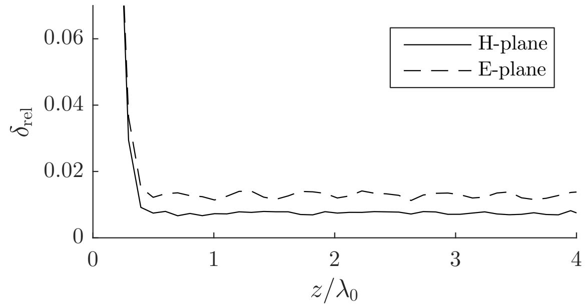

(a)

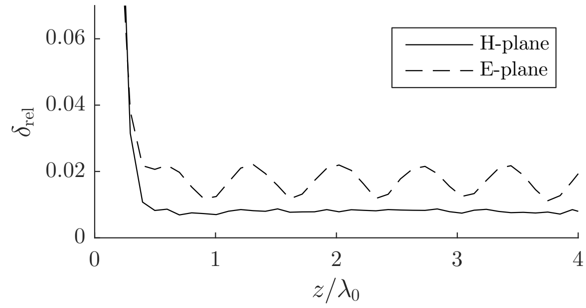

(b)

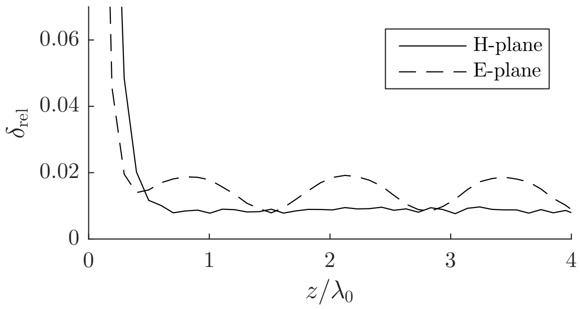

(c)

Figure 4.1: The relative difference between the finite element representation and the plane wave representation of the electric field for some different scan angels, as a function of the distance z above the patch: (a) $\theta = 22.5°$; (b) $\theta = 45°$; and (c) $\theta = 67.5°$.

where $\boldsymbol{E}^{\mathrm{FE}}(x, y, z)$ is the finite element representation given by the COMSOL FEM solver and $\boldsymbol{E}^{\mathrm{PW}}(x, y, z)$ is a single plane wave representation calculated from the finite element solution at a large distance $L_z = 8\lambda_0$ from the antenna:

$$\boldsymbol{E}^{\mathrm{PW}}(x, y, z) = \boldsymbol{E}_{00}^{\mathrm{PW}}\Big|_{z=L_z} e^{-j(k_x^s x + k_y^s y + k_z z)} \tag{4.3}$$

where $\boldsymbol{E}_{00}^{\mathrm{PW}}$ is the plane wave decomposition defined in (3.15).

Figure 4.1a–4.1c show δ_{rel} for some different scan angles, where we note that δ_{rel} is large for $z < 0.4\lambda_0$ due to the decaying evanescent fields and that δ_{rel} does not decrease further for $z > 0.4\lambda$. It is worth to notice that the relative error has a periodic variation in z for large scan angles. The frequency of the oscillations depends only on θ where as the amplitude depends on both scan angles θ and ϕ. The periodicity is explained by reflections due to discretisation errors in the radiating boundary condition (3.10).

The θ and ϕ dependence of δ_{rel} is further studied in Figure 4.2 at $z = 0.43\lambda_0$. We see that the relative difference δ_{rel} is less than 2 % for all angles ϕ when $\theta < 70°$, and for scan-angels $\theta > 70°$, δ_{rel} rapidly increases.

Another way to investigate the necessary height of the unit cell is to perform repeated calculation with different unit cell heights. In Figure 4.3, these results are compared with known results for the same antenna array design studied by Pozar

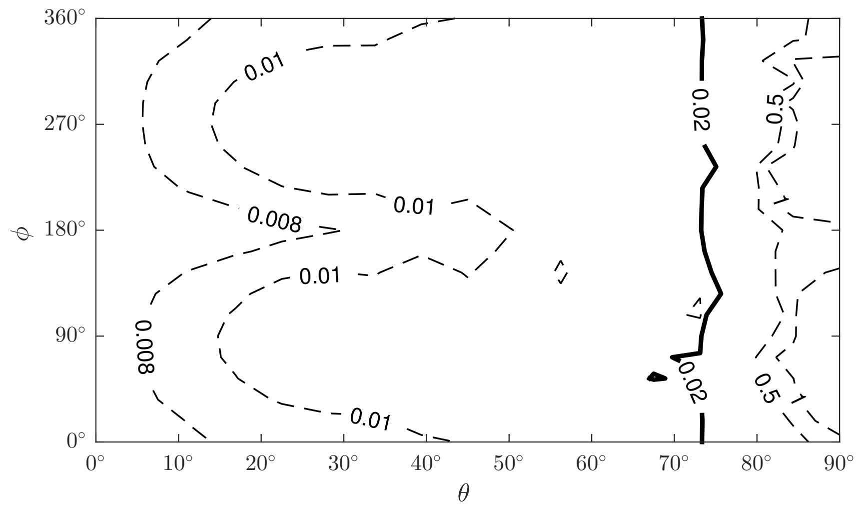

Figure 4.2: The relative difference $\delta_{\text{rel}}(z)$ at $z = 0.43\lambda_0$ for all scan angles. The relative difference is less than 2 % for all angles ϕ when $\theta < 70°$. For angles θ larger than 70°, the relative difference rapidly increases. $\phi = 0° \Leftrightarrow$ H-plane, $\phi = 90° \Leftrightarrow$ E-plane.

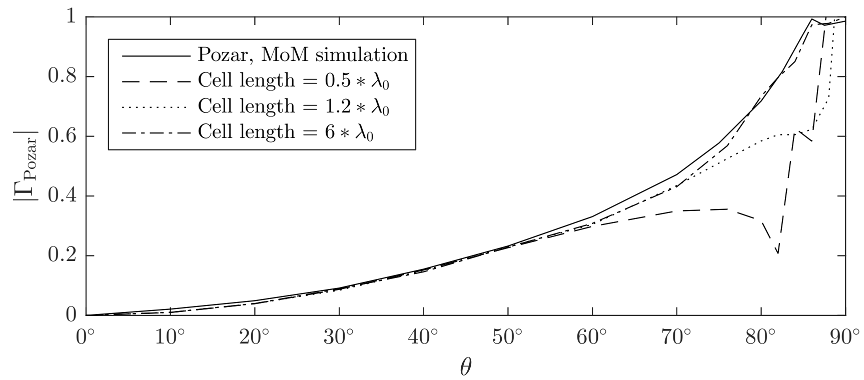

Figure 4.3: E-plane, active reflection coefficient as calculated by Pozar [14] and with COMSOL, FEM simulations for different height of the computational unit cell.

[14]. We see that a unit cell height of at least $1.2\lambda_0$ is required to get a good correspondence for scan-angles $\theta \leq 70°$.

4.1.2 Method validation

In order to test and validate the FEM as implemented and used in COMSOL, we consider the two previously mentioned test problems PA. 1 and PA. 2 that feature infinite planar arrays of rectangular microstrip patches. The active reflection coefficient calculated from the COMSOL FEM simulation is compared to the MoM results from Pozar [14].

In Figure 4.4, the comparison of the active reflection coefficient is shown for PA. 1. There is good correspondence between the results for all scan angles.

Figure 4.5 shows the results for PA. 2. The active reflection coefficient from the COMSOL FEM simulation has good agreement to the Mom results form Pozar [14] up to $\theta = 70°$. There are large errors in the COMSOL simulation for larger scan

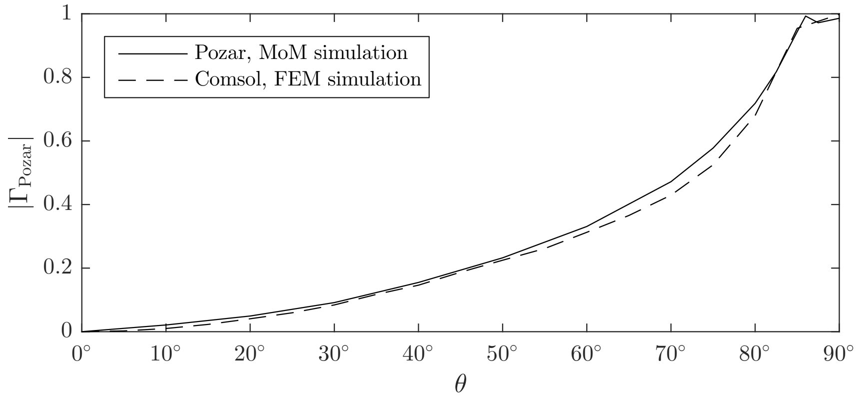

Figure 4.4: A comparison of the E-plane, active reflection coefficient Γ as defined in (4.1), for case PA. 1 without grating lobes.

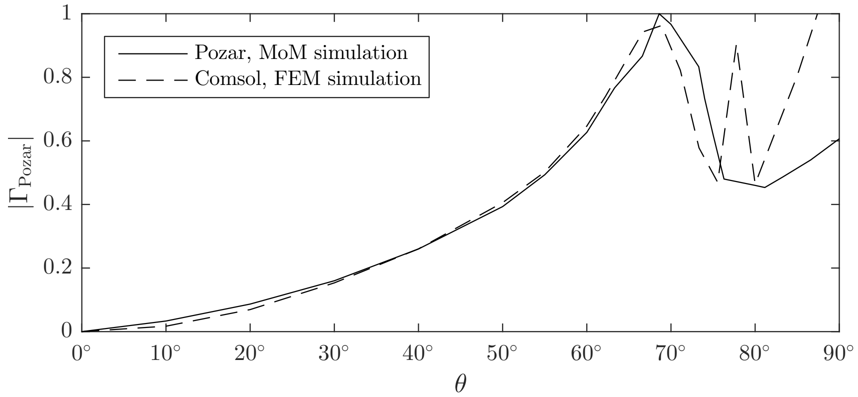

Figure 4.5: A comparison of the E-plane, active reflection coefficient Γ as defined in (4.1), for case PA. 2. The non-unity reflection coefficient at $\theta = 90°$ is explained by a grating lobe created by the $0.51\lambda_0$ unit cell spacing in the y-direction. The COMSOL FEM simulation is not set up to handle grating lobes.

angles due to the presence of grating lobes, which the radiation boundary condition (3.10) can't handle.

4.1.3 Estimation of the numerical error

Numerical tools and simulations never give the exact answer. It is important to estimate the error to ensure that its magnitude is acceptable. The accuracy of the numerical solution depends on the resolution of the computational mesh. Especially sharp corners with singular electromagnetic fields may be problematic and reduce the accuracy of the solution. In our case, we have such singularities along the sharp corners and edges of the microstrip patch. A simple method to estimate the error due to the singular field, is to increasing the resolution of the computational mesh near the these sharp edges and do a convergence test for the error contribution from the singular field. The mesh further away from the patch is left unchanged.

To find out the approximate order of convergence we use the average cell height

h_{avg} of the triangular elements along the side of the patch:

$$h_{\text{avg}} = \left(\frac{2h_{\text{patch}} l_{\text{patch}}}{N}\right)^{1/2} \tag{4.4}$$

where h_{patch} and l_{patch} is the height and with of the patch and N is the total number of cells along a side of the patch.

To estimate the error and the order of convergence, the simulation results I_{num} are fitted to

$$I_{\text{num}} = I_0 + I_\alpha h_{\text{avg}}^\alpha \tag{4.5}$$

where I_0 is the extrapolated value for zero cell size along the sides of the patch and α is the estimated order of convergence.

For the active reflection coefficient ($I_{\text{num}} = \mathit{\Gamma}$) this method yields an order of convergence $\alpha \approx 2.9$ for all scan angles ϕ and $\theta \leq 70°$. Figure 4.6 shows $|\mathit{\Gamma}_{\text{num}}|$ and the extrapolation to zero cell size $|\mathit{\Gamma}_0|$ for the case E-plane and $\theta = 45°$.

We can now make an estimate of the relative error

$$e_{\text{rel}} = \left|\frac{\mathit{\Gamma}_{\text{num}} - \mathit{\Gamma}_0}{\mathit{\Gamma}_0}\right| \tag{4.6}$$

As shown in Figure 4.7, approximate three elements along the height of the patch are needed to get the estimated relative error below 5 %. This mesh resolution near edges and sharp corners are used for the array antenna studied in the next section, the connected slot array antenna.

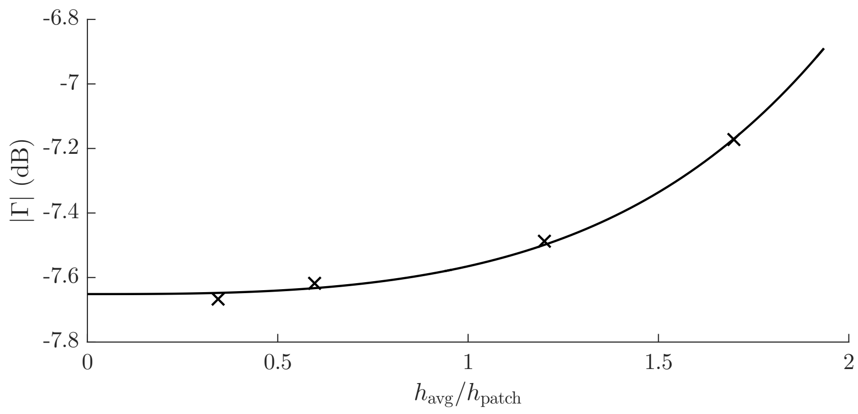

Figure 4.6: Active reflection coefficient $\mathit{\Gamma}$ with extrapolated values as a function of the ratio between the average mesh element side length h_{avg} and the length of the patch. Order of convergence is estimated to 2.9. Scan angle $\theta = 45°$ in the E-plane.

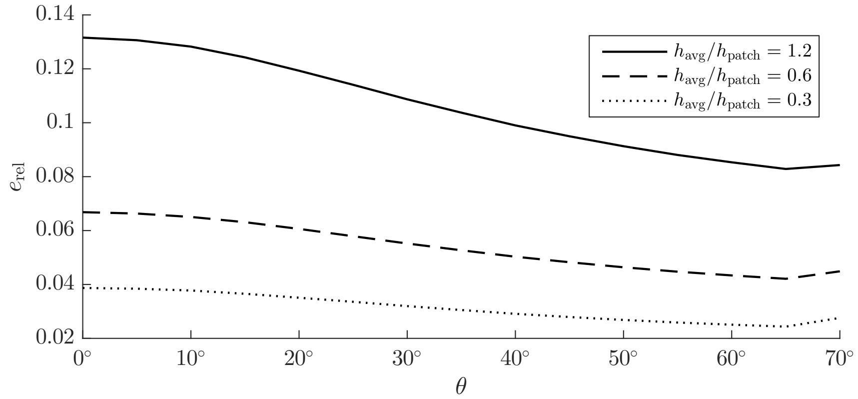

Figure 4.7: An estimate of the relative error $e_{\rm rel}$ for Γ as a function of scan angle in the H-plane for the three different computational meshes with approximate 1, 2 and 3 elements respectively along the height of the microstrip patch.

4.2 Connected slot array antenna

In this section we present results from FEM simulations of the nominal connected slot array (CSA) antenna design described in section 2.6. These results are compared with other similar results in the open literature. Finally, we present some improvements and optimization of the nominal design.

4.2.1 Active reflection coefficient

The active reflection coefficient of the nominal CSA antenna is shown in Figure 4.8 for the E-plane and H-plane. The antenna has an active reflection coefficient that is less than -8 dB in the frequency range 5 GHz to 12 GHz for $\theta < 60°$ in the E-plane and $\theta < 70°$ in the H-plane. The reflection increases rapidly for frequencies below 5 GHz and for higher angles of θ. A scan blindness due to surface waves occur for higher frequencies and scan angles, seen as a dark ridge in the upper right part in Figure 4.8a and 4.8b.

4.2.2 Radiated fields

The radiated power of the co-polarized field is calculated from the far-field plane wave representation

$$E_{\rm co} = \boldsymbol{E}_{00}^{\rm PW} \cdot \hat{\boldsymbol{\imath}}_{\rm co} \tag{4.7}$$

$$P_{\rm co} = \frac{L_x L_y}{2\eta} |E_{\rm co}|^2 \tag{4.8}$$

where the plane wave amplitude $\boldsymbol{E}_{00}^{\rm PW}$ is calculated at $z = L_z$. The efficiency ratio $P_{\rm co}/P_{\rm i}$ where $P_{\rm i}$ is the incident power on the antenna port, is shown in Figure 4.9.

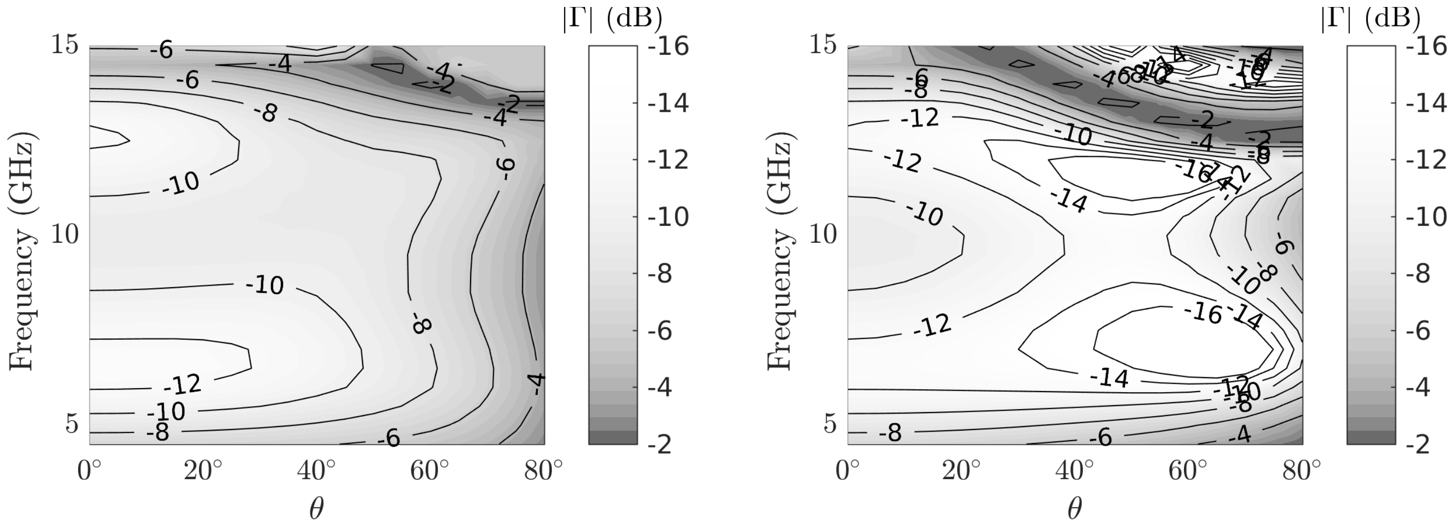

(a) **(b)**

Figure 4.8: The active reflection coefficient $|\Gamma|$ for the nominal connected slot antenna as a function of frequency and scan angle: (a) E-plane; and (b) H-plane.

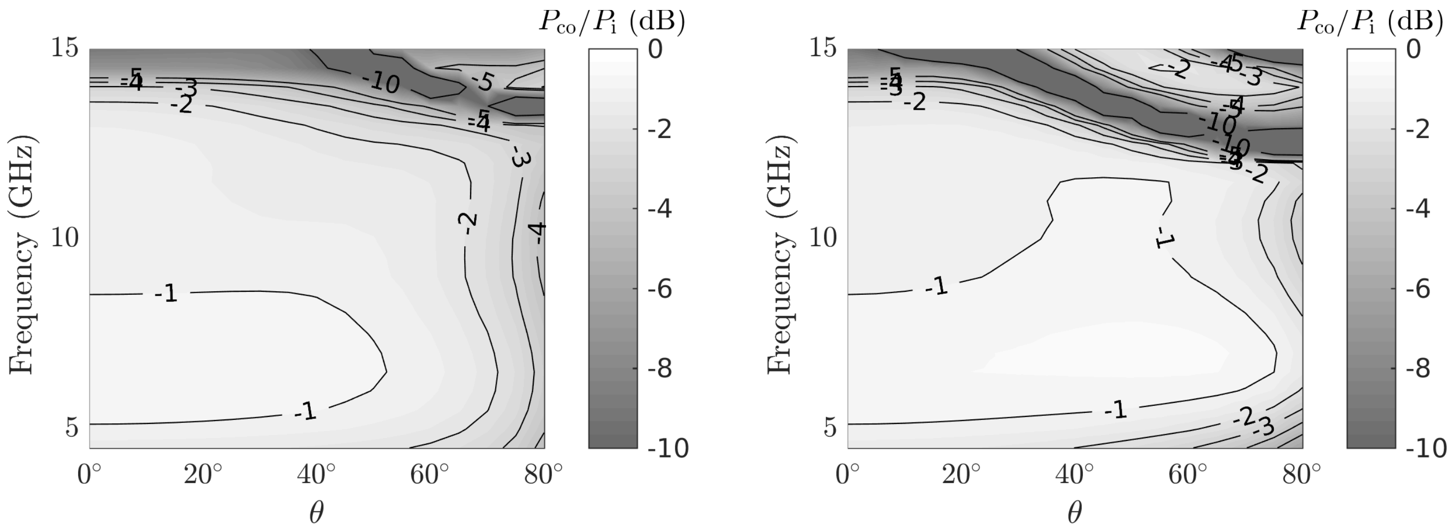

(a) **(b)**

Figure 4.9: The outgoing co-polarized radiated power from the antenna normalised with incident power, i.e. the power efficiency of the antenna: (a) E-plane; and (b) H-plane.

4.2.3 Phase and group propagation

Ideally, both the phase and group delays are constant, i.e. a linear phase shift. Otherwise, a signal that consists of multiple frequency components suffers from distortion. The group and phase time delay of the antenna system can be calculated from the phase shift φ as

$$\tau_{\mathrm{g}}(\omega) = -\frac{d\varphi(\omega)}{d\omega} \tag{4.9}$$

$$\tau_{\mathrm{p}}(\omega) = -\frac{\varphi(\omega)}{\omega} \tag{4.10}$$

The phase shift of the antenna, from the port to the end of the unit cell, is shown in Figure 4.10 for some arbitrary scan angles. With the exception of the scan blindness occurring at higher frequencies, the phase shift is nearly linear. The resulting group delay and phase delay is shown in Figure 4.11 and 4.12. Apart from the scan blindness region, both the group and phase delay is nearly constant at $\tau_{\mathrm{g}} \approx \tau_{\mathrm{p}} \approx 0.1\,\mathrm{ns}$

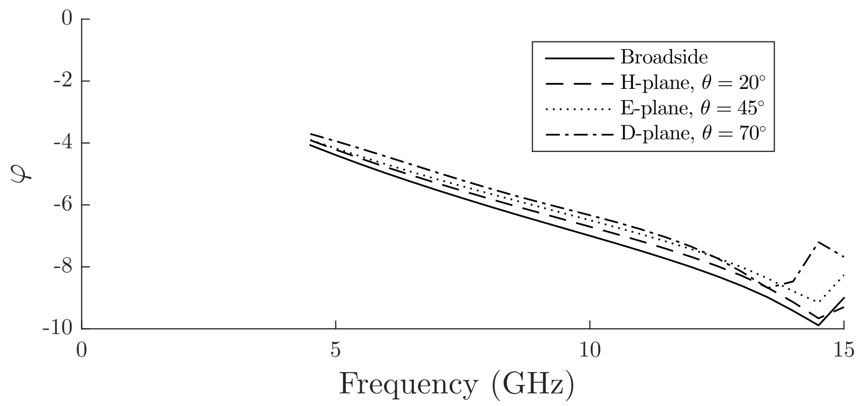

Figure 4.10: The phase shift φ, from the coaxial port to the end of the unit cell, for some different scan angles. The phase is nearly linear everywhere except at the scan blindness occurring around $13 - 15\,\mathrm{GHz}$.

4.2.4 Ohmic, dielectric & polarization losses

Previously, we presented losses due to reflection, i.e. impedance mismatch. Further losses in the antenna are losses due to (i) ohmic resistance associated with metal parts, (ii) dissipation in the dielectric layers and (iii) power radiated in unwanted cross-polarization. The simulation predict negligible ohmic losses. They are less than $3\,\%$ of the net power P_{p} through the port or less than $1.5\,\%$ of the incident power P_{i}.

Figure 4.13 shows the losses due to dissipation in the dielectric layers. These losses are much larger than the ohmic losses and are of the same magnitude as the reflection losses. The dielectric losses increase with higher frequency as expected.

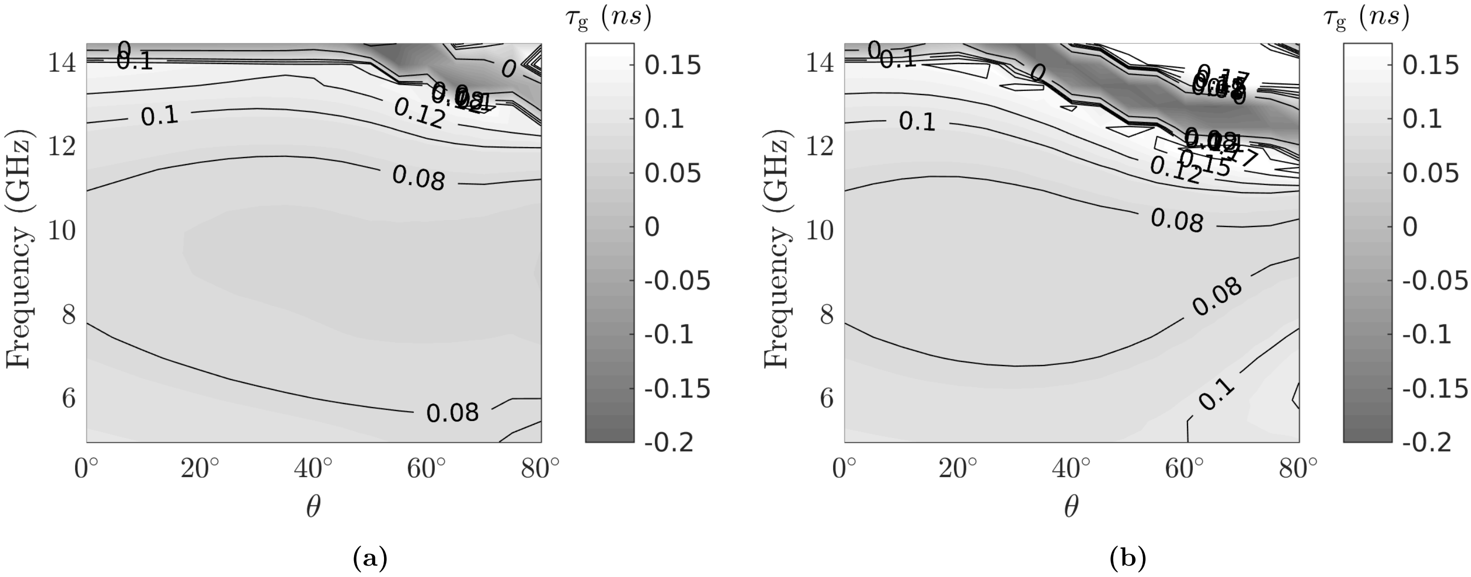

Figure 4.11: The group delay $\tau_g(\omega) = -d\varphi/d\omega$ is the time delay of the amplitude envelope. The group delay is more or less constant at ≈ 0.1 ns apart from the scan blindness region. (a) E-plane; and (b) H-plane.

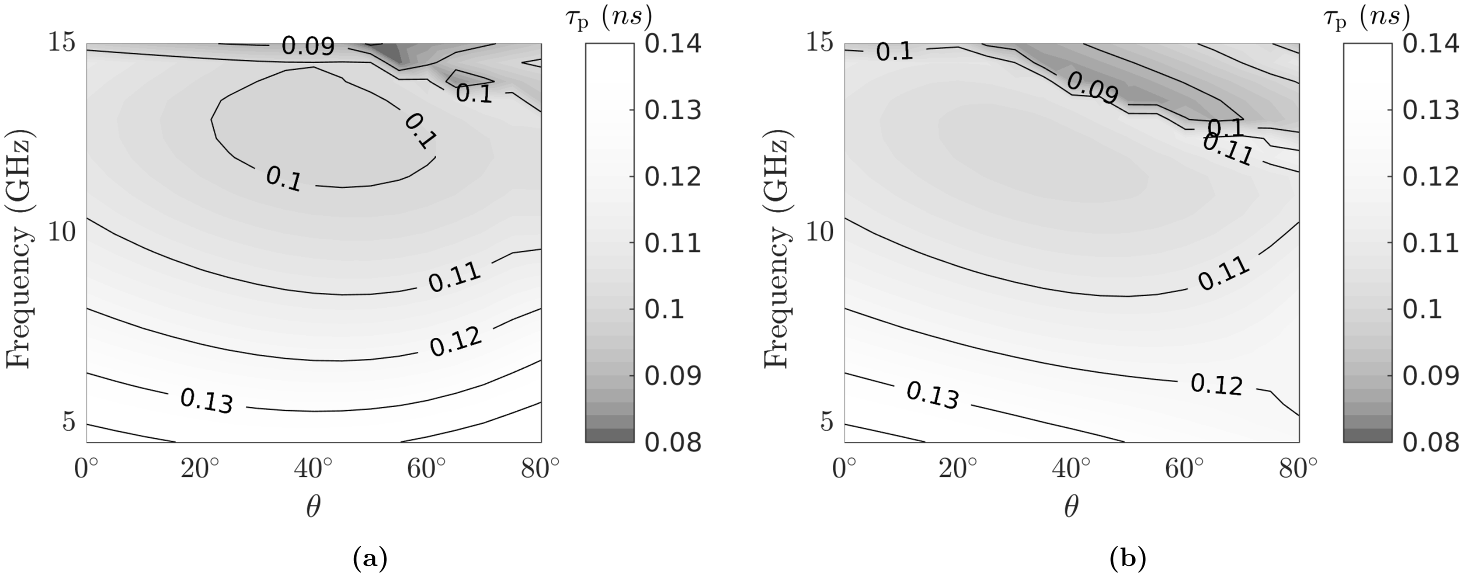

Figure 4.12: The phase delay $\tau_p(\omega) = -\varphi/\omega$. (a) E-plane; and (b) H-plane.

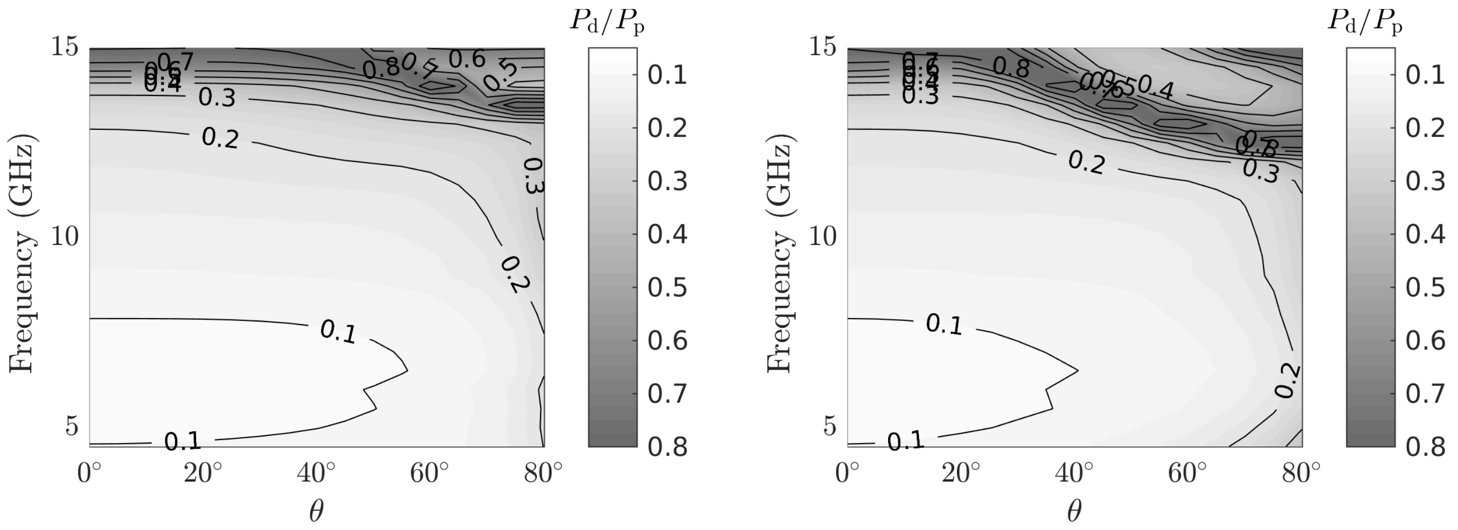

(a) **(b)**

Figure 4.13: The total dielectric losses P_d of the nominal antenna design, as a function of frequency and scan angle. The losses are normalised with the power entering the antenna port $P_p = P_i - P_r$: (a) E-plane; and (b) H-plane.

The cross-polarisation (X-pol) level can be quantified by the *relative cross-polarization level*

$$(XP)_{\mathrm{dB}} = 10 \log \left| \frac{E_{\mathrm{cross}}}{E_{\mathrm{co}}} \right|^2 \tag{4.11}$$

The X-pol level for a linearly polarized antenna is ideally zero in the H- and E-planes and nonzero in the D-plane. For the nominal antenna design, the X-pol levels are indeed very small for the E-plane, less than −80 dB. Figure 4.14 shows that the X-pol level is somewhat higher in the H-plane and the highest values of −5 dB are found in the D-plane. This corresponds to a worst case with 25 % of the total outgoing energy lost in the cross-polarisation which is equivalent to 16 % of the incident power P_i.

4.2.5 Comparison with similar antennas

An antenna design very similar to the one CSA antenna presented here have been studied in [5]. The main difference of this antenna is the use of artificial dielectric layers (ADLs, see section 2.5.3) for the dielectric superstrates. The ADLs consists of arrays of electrically small metallic patches included in a dielectric host medium. The analysis method also differ as a spectral method using the analytical spectral solutions of connected arrays and ADLs are used instead of FEM.

Figure 4.15 shows the voltage standing wave ratio (VSWR) of both antennas as well as a version of the nominal antenna with anisotropic dielectric layer. The performance of the ADL antenna and the nominal antenna are similar, but the VSWR of the nominal antenna is downshifted about 1 Ghz. The largest difference is the scan blindness the nominal antenna exhibits. A possible explanation for

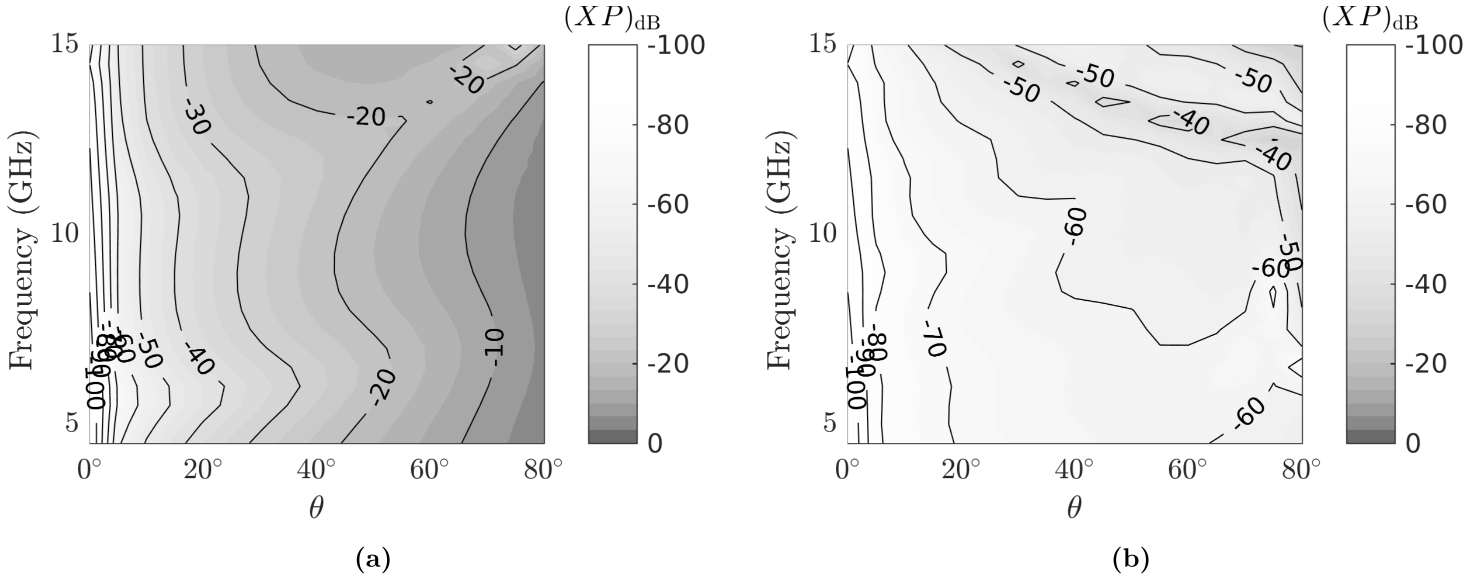

Figure 4.14: Relative cross-polarization level, XP in dB: (a) D-plane; and (b) H-plane.

the scan blindness is surface waves in the dielectric layers. ADLs are supposed to reduce such surface waves. As the isotropic dielectric slabs of the nominal antenna are replaced by anisotropic dielectrics in order to better resemble ADLs, we find that the antenna performance is somewhat improved but it does not mitigate the scan blindness problem.

4.2.6 Design improvements and optimization

To get a single valued figure of merit for the antenna performance, we formulate the following objective function

$$g(G, \boldsymbol{p}) = \left[\frac{1}{3} \sum_{i=1}^{3} \frac{1}{\theta_2 - \theta_1} \int_{\theta_1}^{\theta_2} \frac{1}{f_2 - f_1} \int_{f_1}^{f_2} |G(f, \theta, \phi_i, \boldsymbol{p})|^2 \,\mathrm{d}f\,\mathrm{d}\theta \right]^{1/2} \tag{4.12}$$

where G is an arbitrary antenna parameter that depends on the design parameter vector $\boldsymbol{p}$. The azimuth angle ϕ_i with $i = 1, 2$ and 3 represent the E-, D- and H-plane. To optimize the antenna performance regarding G, we use the finite-difference gradient $dg/d\boldsymbol{p}$ with respect to the design parameters. Table 4.1 lists the design parameters included in $\boldsymbol{p}$. All other design parameters are held constant.

To maximize the power radiated from the antenna, we want to find the minimum of the objective function g with respect to the total losses, i.e. $G = 1 - P_{\mathrm{co}}/P_{\mathrm{i}}$. Figure 4.16 shows parameter sweeps of $g(1 - P_{\mathrm{co}}/P_{\mathrm{i}})$. It is clear that reducing the width of the unit cell is the single most effective measure to improve the antenna performance. A smaller unit cell mitigates the scan blindness problem by shifting it to higher frequencies. With a unit cell width of $0.35\lambda_0$, the VSWR are below 2 for all frequencies $6.5 - 14.5$ GHz within a scanning range of $\pm 60°$ in all azimuth planes. Figure 4.17 shows that the VSWR performance of the antenna with the

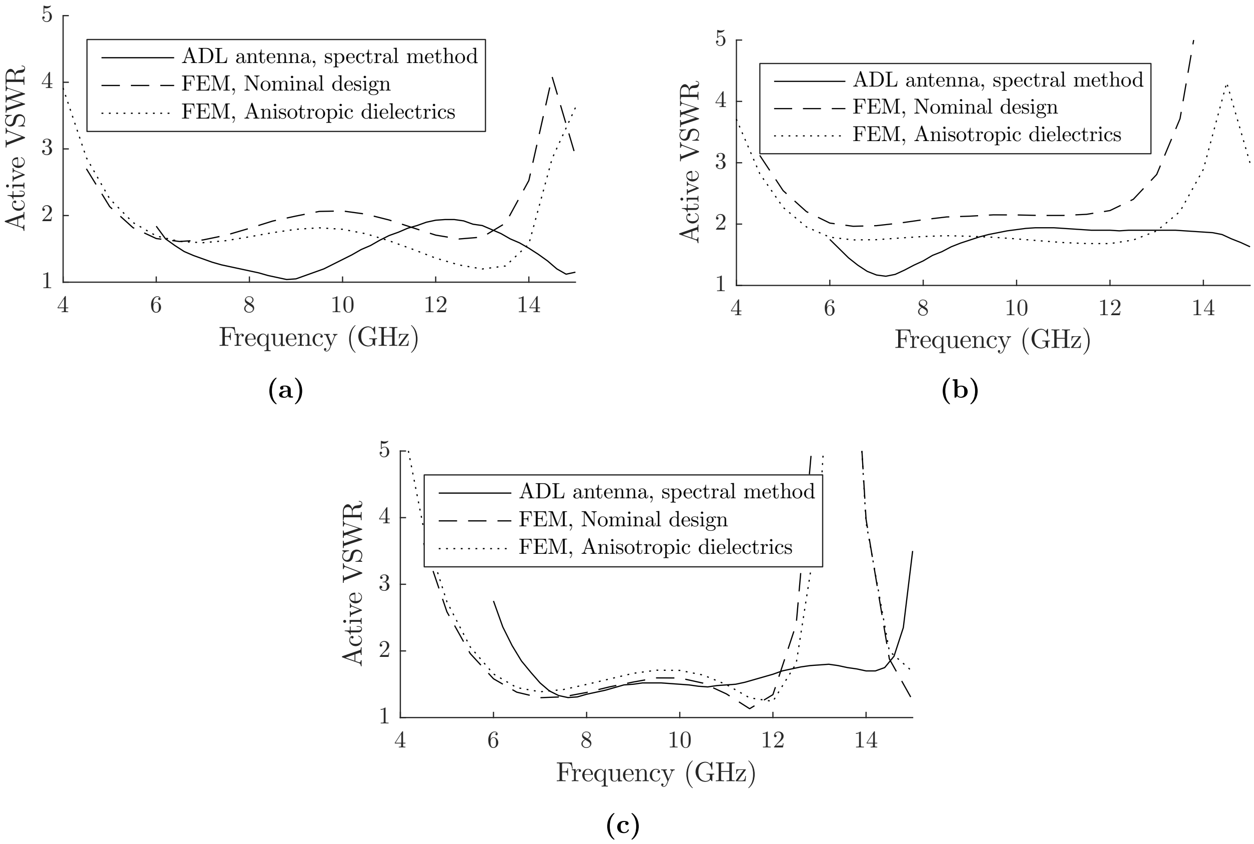

Figure 4.15: A comparison of the active VSWR between the ADL antenna studied in [5] and the nominal antenna with isotropic and anisotropic dielectric slabs for: (a) Broadside; (b) $\theta = 50°$ E-plane; and (c) $\theta = 50°$ H-plane.

smaller unit cell is comparable to the ADL antenna [5], but achieved with normal dielectric superstrates.

Table 4.1: The antenna design parameters spanning the vector $\boldsymbol{p}$ allowed to vary in the object function $g(\boldsymbol{p})$. All other parameters are held constant.

h_{gap1}	Height of gap between array plane and first dielectric slab.
h_{gap2}	Height of gap between dielectric slab 1 and 2
h_{gap3}	Height of gap between dielectric slab 2 and 3
$h_{\text{to\_array}}$	Height from ground plane to the top of the array plane
h_{slab1}	Height of dielectric slab 1
h_{slab2}	Height of dielectric slab 2
h_{slab3}	Height of dielectric slab 3
l_{feed}	Length of microstrip feed line
w_{s}	Width of sloth
L_x	Width of the unit cell, $L_x = L_y$

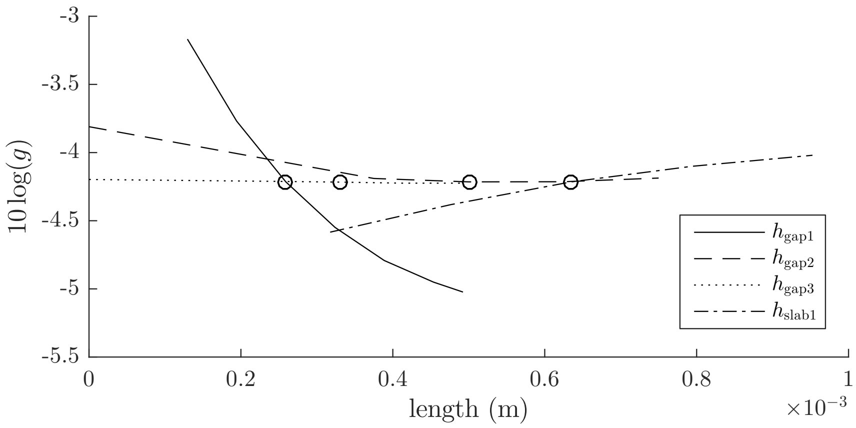

(a)

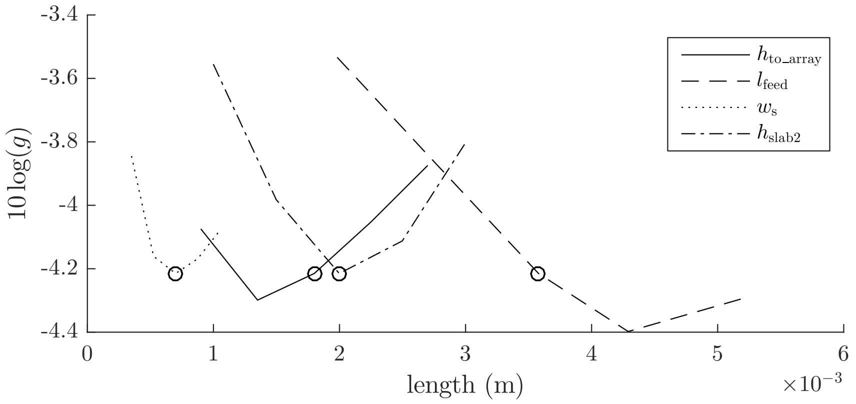

(b)

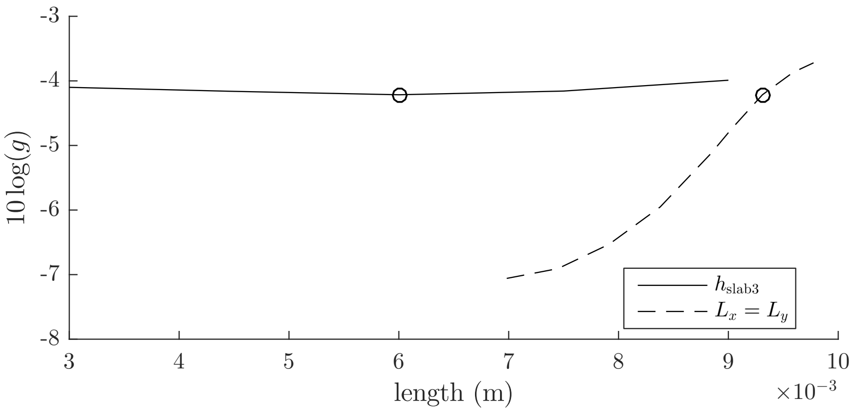

(c)

Figure 4.16: Parameter sweeps of the integrated total losses of the antenna, $g(1 - P_{\text{co}}/P_{\text{i}})$. The integration limits are $5 - 15\,\text{GHz}$ and $0° - 70°$. The circles in the figures mark the nominal antenna design.

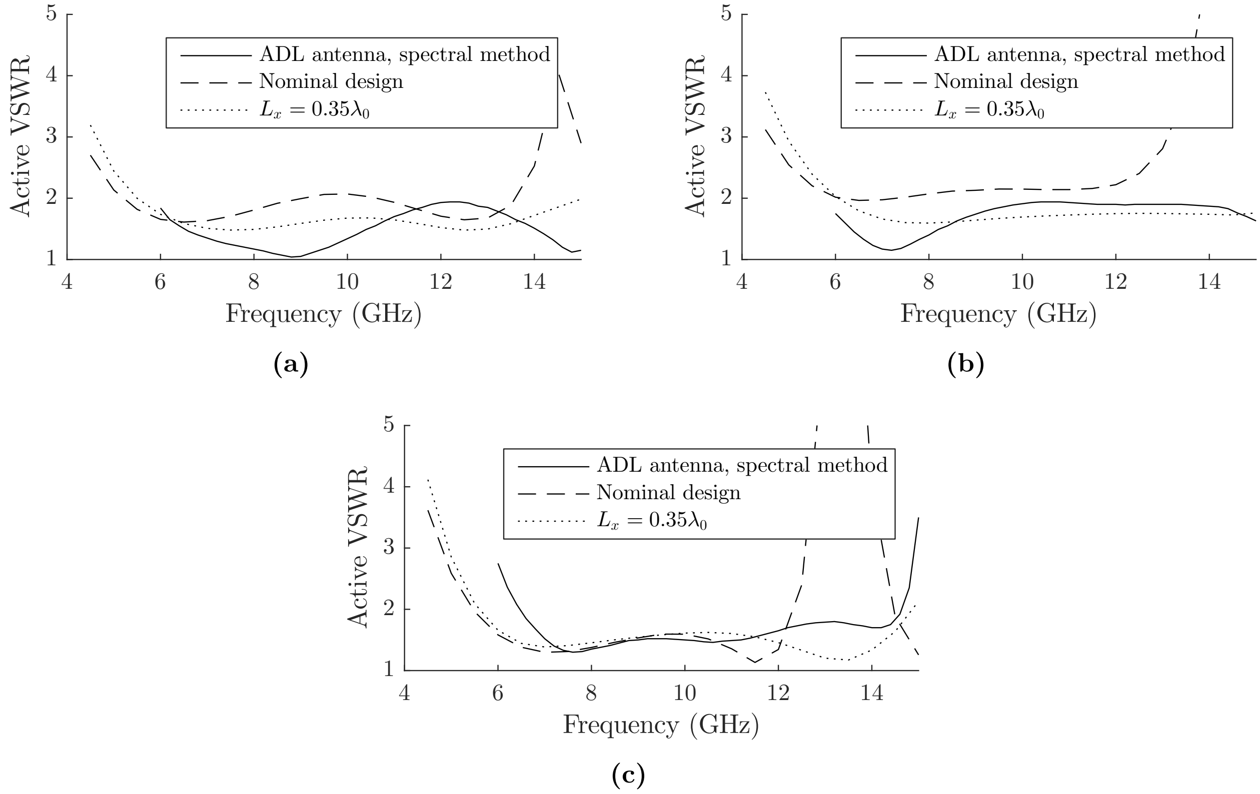

Figure 4.17: A comparison of the active VSWR between the ADL antenna studied in [5] and the nominal antenna and the antenna with reduced unit cell width: (a) Broadside; (b) $\theta = 50°$ E-plane; and (c) $\theta = 50°$ H-plane.

5
Conclusion

In this thesis, we have modelled and studied two types of array antennas with the finite element method. Comparison of the patch antenna with known results shows that the model is valid as long as the width of the unit cell is less than $\lambda_0/2$ such that no grating lobes are present.

Second order curl-conforming basis function have a known order of convergence of 4. Singularities and sharp corners reduces this order of convergence. Trough local refinement along sharp edges and corners the order or convergence was restored to ≈ 2.9. The mesh resolution was chosen so that the estimated error from singularities at sharp corners was kept at approximately $5\,\%$. Preferably, an adaptive mesh refinement method would have been used. This was unfortunately not possible due to restrictions in the available computer resources.

The boundary of the far-field region have been investigated to know where to truncate the unit cell. A distance of $1.2\lambda_0$ from the antenna to the truncating surface is found to be enough to ensure small errors for all scan angle $\theta \leq 70°$.

The initial connected slot array antenna design shows problem with scan blindness due to surface waves. Replacing the isotropic dielectric superstrates with anisotropic ones to simulate ADLs does not suppress the surface waves. Thus, this approach fails to reproduce the result from [5] where ADLs are shown to suppress the surface waves.

The width of the unit cell is the single most effective parameter to reduce the scan blindness. With a smaller unit cell, the surface waves are excited at higher frequencies, thus extending the bandwith of the antenna. The proposed design with an array element spacing of $0.35\lambda_0$ achieves more than one octave bandwidth ($6.5 - 14.5\,\mathrm{GHz}$) within a scanning range of $\pm 60°$ in all azimuth planes.

Bibliography

[1] C. Dehos et al. "Millimeter-wave access and backhauling: the solution to the exponential data traffic increase in 5G mobile communications systems?" In: *IEEE Communications Magazine* 52.9 (Sept. 2014), pp. 88–95. ISSN: 0163-6804. DOI: 10.1109/MCOM.2014.6894457.

[2] R.W. Kindt and W.R. Pickles. "Ultrawideband All-Metal Flared-Notch Array Radiator". In: *Antennas and Propagation, IEEE Transactions on* 58.11 (Nov. 2010), pp. 3568–3575. ISSN: 0018-926X. DOI: 10.1109/TAP.2010.2071360.

[3] R. Kindt and M. Vouvakis. "Low-cost end-point modular PUMA array". In: *Antennas and Propagation USNC/URSI National Radio Science Meeting, 2015 IEEE International Symposium on*. July 2015, pp. 2513–2514. DOI: 10.1109/APS.2015.7305645.

[4] J.T. Logan et al. "A review of Planar Ultrawideband Modular Antenna (PUMA) Arrays". In: *Electromagnetic Theory (EMTS), Proceedings of 2013 URSI International Symposium on*. May 2013, pp. 868–871.

[5] W.H. Syed et al. "Wideband, Wide-Scan Planar Array of Connected Slots Loaded With Artificial Dielectric Superstrates". In: *Antennas and Propagation, IEEE Transactions on* 64.2 (Feb. 2016), pp. 543–553. ISSN: 0018-926X. DOI: 10.1109/TAP.2015.2507167.

[6] B. Riviere et al. "Ultrawideband multilayer printed antenna arrays with wide scanning capability". In: *Antennas and Propagation USNC/URSI National Radio Science Meeting, 2015 IEEE International Symposium on*. July 2015, pp. 514–515. DOI: 10.1109/APS.2015.7304643.

[7] A. Ludwig. "The definition of cross polarization". In: *IEEE Transactions on Antennas and Propagation* 21.1 (Jan. 1973), pp. 116–119. ISSN: 0018-926X. DOI: 10.1109/TAP.1973.1140406.

[8] Sergey V. Yuferev and Nathan Ida. "Surface Impedance Boundary Conditions, A Comprehensive Approach". In: CRC Press, 2009. Chap. 1. ISBN: 978-1-4200-4490-4.

[9] A. Mohsen. "On the impedance boundary condition". In: *Applied Mathematical Modelling* 6.5 (1982), pp. 405–407. ISSN: 0307-904X. DOI: http://dx.doi.org/10.1016/S0307-904X(82)80109-1. URL: http://www.sciencedirect.com/science/article/pii/S0307904X82801091.

[10] W. H. Syed and A. Neto. "Front-to-Back Ratio Enhancement of Planar Printed Antennas by Means of Artificial Dielectric Layers". In: *IEEE Transactions on Antennas and Propagation* 61.11 (Nov. 2013), pp. 5408–5416. ISSN: 0018-926X. DOI: `10.1109/TAP.2013.2275915`.

[11] Thomas Rylander, Pär Ingelström, and SpringerLink (e-book collection). *Computational electromagnetics*. English. Second;2nd 2013; vol. 51. New York, N.Y: Springer, 2013. ISBN: 146145350X;9781461453505;

[12] *COMSOL Multiphysics®*. `https://www.comsol.se/`. Accessed: 2016-07-05.

[13] Jian-Ming Jin et al. *Finite element analysis of antennas and arrays*. English. 1st ed. Hoboken, N.J: John Wiley & Sons, 2009;2008; ISBN: 0470401281.

[14] D. Pozar and D. Schaubert. "Analysis of an infinite array of rectangular microstrip patches with idealized probe feeds". In: *IEEE Transactions on Antennas and Propagation* 32.10 (Oct. 1984), pp. 1101–1107. ISSN: 0018-926X. DOI: `10.1109/TAP.1984.1143211`.